A meshless IRBFN-based numerical simulation of adiabatic shear band formation in one dimension

P. LE[a], N. MAI-DUY[b], T. TRAN-CONG[c], G. BAKER[d]

[a,b,c] Computational Engineering and Science Research Centre (CESRC), University of Southern Queensland, Toowoomba Qld 4350, Australia
lephong@usq.edu.au/maiduy@usq.edu.au/trancong@usq.edu.au
[d] Deputy Vice-Chancellor (S), University of Southern Queensland, Toowoomba Qld 4350, Australia
bakerg@usq.edu.au

Abstract

In this paper, we describe an integrated radial basis function network (IRBFN) method for the numerical modelling of the dynamics of strain localization in elasto-thermo-viscoplastic materials with coupled heat conduction. A new coordinate mapping for the IRBFN method is introduced in this paper to resolve the steep temperature, velocity, strain and strain-rate gradients associated with the strain localization (shear band). The discrete governing PDEs are integrated in time using an implicit 5^{th}-order Runge-Kutta method with automatic time step selection. Numerical results demonstrate the efficiency of the present IRBFN approach in solving steep (singularity-like behaviour) nonlinear PDEs encountered.

Introduction

Strain localization in elasto-thermo-visco-plastic materials is a phenomenon that occurs during high strain-rate plastic deformation, such as machining, forging, shock impact loading, ballistic impact and penetration, and has been proposed as an explanation for deep earthquakes [1]. In particular, a shear band is a narrow, nearly planar or two dimensional region of very large shear strain and strain rate. The formation of shear bands often precedes the rupture in materials. Even when the rupture does not occur, the development of shear bands generally reduces the performance of the material. Hence, an understanding of shear-band morphology and evolution is an important prerequisite to improve material processes and manufacturing techniques. Shear bands are commonly of isothermal or adiabatic types. Isothermal shear bands form as a result of strain softening, and thermal softening plays a negligible role in the process. On the other hand, adiabatic shear bands, in which thermal softening plays a primary role, form as a result of an autocatalytic process: an increase in strain rate in a weaker zone causes a local increase in temperature which in turn creates a further increase in strain rate. Once a band is fully formed, the two sides of the region are displaced relative to each other, much like a mode II or mode III crack, but the material still retains full physical continuity from one side to the other.

This paper focuses on adiabatic shear bands. The equations governing the evolution of adiabatic shear bands are coupled, highly nonlinear and stiff, and it is not simple, even for one-dimensional problems, to obtain close form solutions that could describe a range of constitutive, boundary, and initial conditions. For a number of special cases, close form exact and approximate solutions have been developed by many authors to capture some of the fundamental characteristics of strain localization. Generally, numerical solutions are helpful

in a parametric study to cover a range of possible behaviours. However, it could be costly to resolve shear bands fully in a large scale computation since the morphology of a shear band exhibits very fine transverse scales, with aspect ratios of the high shear region usually in the hundreds or even thousands. Thus it is highly desirable to have effective and efficient numerical methods for the analysis of strain localisation problems. The spectral method [2] is particularly effective and efficient, but generally restricted to simple geometries. The finite element method (FEM) [1, 3, 4] has been used to analyze shear strain localization problems with good results for 1D cases, since the Lagrangian finite element mesh is not badly distorted and small element size of $O(10^{-7})$ enables one to capture the high strain. However, the FEM has many drawbacks in 2D or 3D strain localization problems. In contrast to the FEM, meshless methods [5, 6] offer some advantages, including (i) shape functions are constructed by using a highly smooth window function, (ii) purely displacement-based formulation is possible without incurring volumetric locking within a range of support size of the window functions [5], and (iii) approximations are non-local. Thus, meshless methods provide more continuous solutions than the piece-wise continuous ones obtained by the FEM. These properties provide an effective remedy for the mesh alignment sensitivity in the computation of strain localization.

In this study, we report a new numerical method based on radial basis function networks, a truly meshless method, for analysis of the dynamics of strain localization in 1D problems. The present indirect/integral radial basis function network (IRBFN) method is based on (i) the universal approximation property of RBF networks, (ii) exponential convergence characteristics of the chosen multiquadric (MQ) RBF, (iii) a simple point collocation method of discretisation of the governing equations, and (iv) an indirect/integral (IRBFN) rather than a direct/differential (DRBFN) approach [7] for the approximation of functions and derivatives. For the DRBFN, Madych and Nelson [8] showed that the convergence rate is a decreasing function of derivative order. Since the introduction of the IRBFN approach by Mai-Duy and Tran-Cong [9, 10], Kansa et al [11], and Ling and Trummer [12], based on the theoretical result of Madych and Nelson [8], concluded that the decreasing rate of convergence can be avoided in the IRBFN approach. Furthermore, the integration constants arisen in the IRBFN approach are helpful in dealing with problems with multiple boundary conditions [13]. In addition, a new coordinate mapping is here introduced to help capture the characteristics of extremely thin localised shear bands.

Strain localisation Problem

An infinite slab of an elasto-thermo-viscoplastic material, with half thickness $\bar{H}$ (the overbar represents dimensional quantities), is subjected to simple shearing in the direction parallel to the slab. The unknowns are the shear stress $\bar{s}$, the particle velocity $\bar{v}$, the plastic strain γ and the temperature measured from the reference value $\bar{\Theta}$. Ψ is a strain hardening parameter. Let $\bar{y}$ be the coordinate across the slab with origin on the middle plane, i.e. $-\bar{H} \leq \bar{y} \leq \bar{H}$, and $\bar{t}$ denote time. The mathematical model for this problem can be found in [1, 2, 6] and is reproduced here as follows.

$$\bar{v}_{,\bar{t}} = \frac{\bar{s}_{,\bar{y}}}{\bar{\rho}},\ \bar{s}_{,\bar{t}} = \bar{\mu}(\bar{v}_{,\bar{y}} - \bar{\gamma}_{,\bar{t}}),\ \bar{\rho}\bar{c}\bar{\Theta}_{,\bar{t}} = \bar{k}\bar{\Theta}_{,\bar{y}\bar{y}} + \bar{s}\bar{\gamma}_{,\bar{t}},\ \bar{\Psi}_{,\bar{t}} = \frac{\bar{s}\bar{\gamma}_{,\bar{t}}}{\bar{\kappa}(\Psi)},\ \bar{s} = \bar{\kappa}(\Psi)g(\bar{\Theta})f(\bar{\gamma}_{,\bar{t}}), \quad (1)$$

where $\bar{\rho}$ is the density, $\bar{c}$ the specific heat, $\bar{k}$ the thermal conductivity, $\bar{\mu}$ the shear modulus, and $\bar{\kappa}$ a strain hardening factor, g a thermal softening factor, and f a strain rate hardening factor. Different material models can be obtained with appropriate choices of the g and

h factors in the constitutive relation. The problem is assumed to be symmetric about the middle plane $\bar{y} = 0$. The slab is subjected to a constant shearing velocity $\pm\bar{v}^0$ prescribed at the top and bottom surfaces of the slab, respectively. The surfaces are thermally insulated and all plastic work is converted into heat. The above assumptions lead to the following boundary conditions

$$\bar{v}(0,\bar{t}) = 0, \qquad \bar{v}(\bar{H},\bar{t}) = \bar{v}_0, \qquad \bar{\Theta}_{,\bar{y}}(0,\bar{t}) = 0, \qquad \bar{\Theta}_{,\bar{y}}(\bar{H},\bar{t}) = 0. \tag{2}$$

The nominal strain rate is $\dot{\bar{\gamma}}^0 = \bar{\gamma}^0_{,\bar{t}} = \bar{v}^0/\bar{H}$, where the time derivatives are from now on indicated by a dot over the variable. The dimensionless variables are $y = \bar{y}/\bar{H}$, $t = \bar{t}\dot{\bar{\gamma}}^0$, $\dot{\Psi} = \dot{\bar{\Psi}}/\dot{\bar{\gamma}}^0$, $v = \bar{v}/\bar{H}\dot{\bar{\gamma}}^0$, $s = \bar{s}/\bar{\kappa}^0$, $\Theta = \bar{\rho}\bar{c}\bar{\Theta}/\bar{\kappa}^0$, $\kappa = \bar{\kappa}/\bar{\kappa}^0$, $\dot{\gamma} = \dot{\bar{\gamma}}/\dot{\bar{\gamma}}^0$, $k = \bar{k}/\bar{\rho}\bar{c}\bar{H}^2\dot{\bar{\gamma}}^0$, $\rho = \bar{\rho}\bar{H}^2(\dot{\bar{\gamma}}^0)^2/\bar{\kappa}^0$, $\mu = \bar{\mu}/\bar{\kappa}^0$, $b = \bar{b}\dot{\bar{\gamma}}^0$, $a = \bar{a}\bar{\kappa}^0/\bar{\rho}\bar{c}$, where $\bar{a}$ is the thermal softening parameter, $\bar{b}$ is the strain-rate hardening parameter, $\bar{\kappa}_0$ is the yield stress in the quasi-static isothermal simple shear test. The dimensionless governing equations are

$$\dot{v} = \frac{s_{,y}}{\rho}, \quad \dot{s} = \mu(v_{,y} - \dot{\gamma}), \quad \dot{\Theta} = k\Theta_{,yy} + s\dot{\gamma}, \quad \dot{\Psi} = \frac{s\dot{\gamma}}{\kappa(\Psi)}, \quad s = \kappa(\Psi)g(\Theta)f(\dot{\gamma}). \tag{3}$$

The boundary conditions are

$$v(0,t) = 0, \quad v(1,t) = 1, \quad \Theta_{,y}(0,t) = 0, \quad \Theta_{,y}(1,t) = 0, \quad s_{,y}(0,t) = 0, \quad s_{,y}(1,t) = 0, \tag{4}$$

where the boundary conditions for shear stress can be easily deduced.

Numerical formulation

Consider an initial-boundary-value problem governed by the second order PDE

$$\frac{\partial u}{\partial t} = a\frac{\partial^2 u}{\partial x^2} + b\frac{\partial u}{\partial x} + cu + d, \tag{5}$$

where a, b, c and d are the coefficients, $0 \le t \le T$ and $x_{min} \le x \le x_{max}$, with the boundary and initial conditions

$$u(t, x_{min}) = u_1, \quad \frac{\partial u}{\partial x}|_{(t,x=x_{max})} = u'_N, \quad u(0,x) = g(x), \tag{6}$$

in which u_1 and u'_N are given values, and $g(x)$ is a known function.

Spatial discretisation

In the indirect RBF method (see [9, 10, 14, 15]), the formulation of the problem starts with the decomposition of the highest order derivative under consideration into RBFs. The derivative expression obtained is then integrated to yield expressions for lower order derivatives and finally for the original function itself. The present work is concerned with the approximation of a function and its derivatives of order up to 2, the formulation can be thus described as follows.

$$\frac{d^2u(x,t)}{dx^2} = \sum_{i=1}^{m} w_i(t)g_i(x) = \sum_{i=1}^{m} w_i(t)H_i^{[2]}(x), \tag{7}$$

$$\frac{du(x,t)}{dx} = \int \sum_{i=1}^{m} w_i(t)g_i(x)dx + c_1(t) = \sum_{i=1}^{m} w_i(t)H_i^{[1]}(x) + c_1(t), \tag{8}$$

$$u(x,t) = \sum_{i=1}^{m} w_i(t) \int H_i^{[1]}(x)dx + c_1(t)x + c_2(t) = \sum_{i=1}^{m} w_i(t) H_i^{[0]}(x) + c_1(t)x + c_2(t), \quad (9)$$

where m is the number of RBFs, $\{g_i(x)\}_{i=1}^m$ is the set of RBFs, $\{w_i(t)\}_{i=1}^m$ is the set of corresponding network weights to be found and $\{H_i^{[.]}(x)\}_{i=1}^m$ are new basis functions obtained from integrating the radial basis function $g_i(x)$. The multiquadrics function is chosen in the present study $g_i(x) = \sqrt{(x-c_i)^2 + a_i^2}$, where c_i is the RBF centre and a_i is the RBF width. The width of the i^{th} RBF can be determined according to the following simple relation $a_i = \beta d_i$, where β is a factor, $\beta > 0$, and d_i is the distance from the i^{th} centre to its nearest centre. To have the same coefficient vector as (9), expressions (7) and (8) can be rewritten as

$$\frac{d^2u(x,t)}{dx^2} = \sum_{i=1}^{m} w_i(t) H_i^{[2]}(x) + c_1(t).0 + c_2(t).0, \quad (10)$$

$$\frac{du(x,t)}{dx} = \sum_{i=1}^{m} w_i(t) H_i^{[1]}(x) + c_1(t).1 + c_2(t).0. \quad (11)$$

Here we choose the RBF centres c_i to be identical to the collocation points x_i, i.e. $\{c_i\}_{i=1}^m \equiv \{x_i\}_{i=1}^N$. The evaluation of (10), (11) and (9) at a set of N collocation points leads to

$$\mathbf{u}''(t) = \mathbf{H^{[2]}}\mathbf{w}(t), \quad \mathbf{u}'(t) = \mathbf{H^{[1]}}\mathbf{w}(t), \quad \mathbf{u}(t) = \mathbf{H^{[0]}}\mathbf{w}(t), \quad (12)$$

where

$$\mathbf{u}''(t) = \left[\frac{\partial^2 u_1(t)}{\partial x^2}, \frac{\partial^2 u_2(t)}{\partial x^2}, \ldots, \frac{\partial^2 u_N(t)}{\partial x^2} \right]^T, \quad (13)$$

$$\mathbf{u}'(t) = \left[\frac{\partial u_1(t)}{\partial x}, \frac{\partial u_2(t)}{\partial x}, \ldots, \frac{\partial u_N(t)}{\partial x} \right]^T, \quad (14)$$

$$\mathbf{u}(t) = [u_1(t), u_2(t), \ldots, u_N(t)]^T, \quad (15)$$

$$\mathbf{H^{[2]}} = \begin{pmatrix} H_1^{[2]}(x_1) & H_2^{[2]}(x_1) & \cdots & H_N^{[2]}(x_1) & 0 & 0 \\ H_1^{[2]}(x_2) & H_2^{[2]}(x_2) & \cdots & H_N^{[2]}(x_2) & 0 & 0 \\ \vdots & \vdots & \ddots & \vdots & \vdots & \vdots \\ H_1^{[2]}(x_N) & H_2^{[2]}(x_N) & \cdots & H_N^{[2]}(x_N) & 0 & 0 \end{pmatrix}, \quad (16)$$

$$\mathbf{H^{[1]}} = \begin{pmatrix} H_1^{[1]}(x_1) & H_2^{[1]}(x_1) & \cdots & H_N^{[1]}(x_1) & 1 & 0 \\ H_1^{[1]}(x_2) & H_2^{[1]}(x_2) & \cdots & H_N^{[1]}(x_2) & 1 & 0 \\ \vdots & \vdots & \ddots & \vdots & \vdots & \vdots \\ H_1^{[1]}(x_N) & H_2^{[1]}(x_N) & \cdots & H_N^{[1]}(x_N) & 1 & 0 \end{pmatrix}, \quad (17)$$

$$\mathbf{H^{[0]}} = \begin{pmatrix} H_1^{[0]}(x_1) & H_2^{[0]}(x_1) & \cdots & H_N^{[0]}(x_1) & x_1 & 1 \\ H_1^{[0]}(x_2) & H_2^{[0]}(x_2) & \cdots & H_N^{[0]}(x_2) & x_2 & 1 \\ \vdots & \vdots & \ddots & \vdots & \vdots & \vdots \\ H_1^{[0]}(x_N) & H_2^{[0]}(x_N) & \cdots & H_N^{[0]}(x_N) & x_N & 1 \end{pmatrix}, \quad (18)$$

$$\mathbf{w}(t) = [w_1(t), ..., w_N(t), c_1(t), c_2(t)]^T. \quad (19)$$

From an engineering point of view, it would be more convenient to work in the physical space. Owing to the presence of integration constants, the process of converting the networks-weight space into the physical space can also be used to implement Neumann boundary conditions. With the boundary conditions (6), the conversion system and its inverse can be employed as

$$\begin{matrix}\mathbf{u}(t)\\ u'_N(t)\end{matrix} = \mathbf{C}\mathbf{w}(t), \quad \mathbf{w}(t) = \mathbf{C}^{-1} \begin{matrix}\mathbf{u}(t)\\ u'_N(t)\end{matrix} \quad . \tag{20}$$

where $\mathbf{C}$ is the conversion matrix of dimension $(N+1)\times(N+2)$ that comprises the matrix $\mathbf{H}^{[\mathbf{0}]}$ and the last row of $\mathbf{H}^{[\mathbf{1}]}$. By substituting (20) into (12), the values of the second and first derivatives of u with respect to x are thus expressed in terms of nodal variable values and Neumann boundary value

$$\mathbf{u}''(t) = \mathbf{H}^{[\mathbf{2}]}\mathbf{C}^{-1} \begin{matrix}\mathbf{u}(t)\\ u'_N(t)\end{matrix} = \mathbf{D}^{[\mathbf{2}]} \begin{matrix}\mathbf{u}(t)\\ u'_N(t)\end{matrix} \quad , \quad \mathbf{u}'(t) = \mathbf{H}^{[\mathbf{1}]}\mathbf{C}^{-1} \begin{matrix}\mathbf{u}(t)\\ u'_N(t)\end{matrix} = \mathbf{D}^{[\mathbf{1}]} \begin{matrix}\mathbf{u}(t)\\ u'_N(t)\end{matrix} \quad . \tag{21}$$

Making use of (21), equation (5) can be transformed into the following discrete form

$$\frac{d\mathbf{u}}{dt} = a\mathbf{D}^{[\mathbf{2}]} \begin{matrix}\mathbf{u}(t)\\ u'_N(t)\end{matrix} + b\mathbf{D}^{[\mathbf{1}]} \begin{matrix}\mathbf{u}(t)\\ u'_N(t)\end{matrix} + c\mathbf{u}(t) + \mathbf{d}, \tag{22}$$

where $\mathbf{d} = [d, d, \ldots d]^T$ is an $N \times 1$ vector, and $\frac{d\mathbf{u}}{dt} = \left[\frac{du_1(t)}{dt}, \frac{du_2(t)}{dt}, \ldots, \frac{du_N(t)}{dt}\right]^T$. Since the values of u_1 and u'_N are given, the unknown vector becomes $[u_2(t), u_3(t), \ldots, u_N(t)]^T$, and hence, the first row in (22) will be removed from the solution procedure. The remainder of (22) can be integrated in time by using standard solvers such as the Runge-Kutta technique.

Resolution of very large spatial gradients

It has been shown that the IRBFN method can capture sharp gradients in some PDE solutions [16] with relatively coarse uniform spatial discretisation. However, with extremely sharp gradients in a solution, the option of uniformly refining the discretisation is not efficient or even effective. The computing of such extremely sharp gradients can be achieved effectively and efficiently with appropriate coordinate mappings of a relatively coarse, originally uniform discretisation. Consider the one-to-one mapping given by $x(y) = \sinh(\alpha y)/\sinh(\alpha)$, where $\alpha > 0$ is a parameter that allows control of the discretisation. This mapping can be illustrated via the following singularly perturbed boundary value problem

$$\epsilon u''(x) + p(x)u'(x) + q(x)u(x) = f(x), \qquad \forall x \in [a, b]\,, \tag{23}$$

subject to the boundary condition $u(a) = u_a, \quad u(b) = u_b$, where $\epsilon > 0$ denotes a fixed small constant. As $\epsilon \longrightarrow 0$ (the smaller the value of ϵ is, the larger the value of α is required), this mapping will enable sufficient resolution of boundary layers of width $O(\epsilon)$, given a relatively coarse uniform discretisation on the computational domain. For example, we have obtained excellent numerical solution to a specific form of (23) with $\epsilon = 10^{-6}$, $\alpha = 13$ and 61 collocation points.

Numerical example

We consider a specific case of the general unidirectional shearing problem defined earlier where the thermal softening factor in (3) is given by $g(\Theta) = (1 - a\Theta)$, the strain hardening

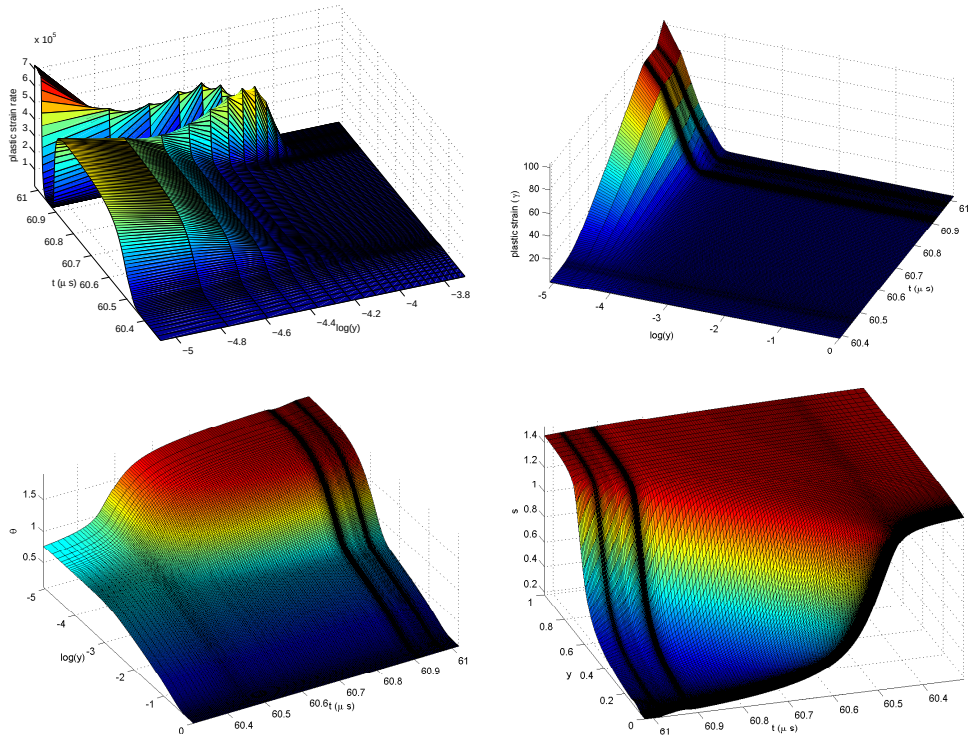

Figure 1: Evolution of the spatial profile of the plastic strain rate ($\dot{\gamma}$), plastic strain (γ), temperature (Θ), and shear stress s

factor by $\kappa(\Psi) = \left(1 + \frac{\Psi}{\Psi^0}\right)^n$, and the strain rate hardening factor by $f(\dot{\gamma}) = (1 + b\dot{\gamma})^m$. For comparison purpose, the initial conditions and boundary conditions are taken to be the same as in [6]. The latter are described earlier by (4) and the former are given by $v(0, y) = y, \quad \Psi(0, y) = 0.1, \quad \gamma = 0.0692, \quad \Theta(0, y) = 0.1003 + 0.1(1 - y^2)^9 e^{-5y^2}, \quad s(0, y) = \left(1 + \frac{0.1}{\Psi^0}\right)^n (1 - a\Theta(0, y))(1 + b)^m$, where the second term on the right-hand side of the expression for the temperature Θ represents a thermal imperfection. With the half thickness of the slab $\bar{H} = 2.58$mm, the nominal strain rate is $\bar{\gamma}^0_{\bar{t}} = 500\text{s}^{-1}$ and the dimensionless parameters are $\rho = 3.982 \times 10^{-5}, \quad \mu = 240.3, \quad a = 0.4973, \quad n = 0.09, \quad \kappa = 3.978 \times 10^{-3}, \quad \Psi_0 = 0.017, \quad m = 0.025, \quad b = 5 \times 10^{-6}$.

The discretisation of the governing equations yields a system of fully coupled, stiff and nonlinear ordinary differential equations (ODEs) which are integrated with respect to time t using an implicit 5^{th} Runge-Kutta method with subroutine RADAU5 developed by Hairer et al [17]. The subroutine automatically adjusts the time step size to compute the solutions within the prescribed accuracy. The results presented in this paper are obtained by setting $RTOL = 10^{-7}$ and $ATOL = 10^{-7}$ in RADAU5.

The results presented in this section are obtained with 261 collocation points and the value

of α in the coordinate mapping is 9, β in formula for RBF widths is 1. The evolutions of the spatial profile of the temperature Θ, plastic strain γ, and strain hardening parameter Ψ,the plastic strain rate, stress and velocity are shown in figures 1 and 2. These figures show that the solution is highly consistent with the boundary conditions at $y = 0$ and at $y = \pm 1$. From figure 2 it can be observed that the plastic strain increases rapidly in the neighbourhood of $y = 0$ where the band of high shear strains becomes less and less diffuse, reaching a minimum with a very high corresponding plastic strain level before becoming more and more diffuse again. Similar patterns of development are observed for the temperature, strain hardening parameter, plastic strain rate and velocity. In contrast, the spatial profile of stress evolves slightly differently which will be discussed in more detail later.

Although banding of high shear strains is apparent, the smooth spatial profiles do not provide a clear and unique bandwidth. Thus we define the limit of the high shear band as the position where the temperature equals 40% of the peak temperature at the centre of the band. The bandwidth evolves with time, for example when the plastic strain rate at $y = 0$ reaches its maximum value (at $t = 60.8385\mu$s), the extent of the corresponding bandwidth is $y = \pm 0.00252$. Hence the width of the shear band is $2 \times 0.00252 \times 2580 = 13.0\mu$m. The dimensionless half bandwidths correspond to different time levels (in parentheses) are 0.0688 (3),0.0257 (4),0.0102 (5),0.00279 (6),0.00237 (7),0.002468 (8),0.00264 (9),0.00274 (10),0.00276 (11), which indicate that the shear band becomes narrowest (around time level 7 or 60.702μs) before the plastic strain rate peaks between time levels 8 (60.804μs) and 9 (60.903μs).

An examination of the evolution of the shear stress and temperature at $y = 0$ shows the shear stress initially increases slightly (from the initial value of 1.575) since strain and strain rate hardening effects are stronger than the thermal softening effect. As time progresses, the increase in plastic work causes increase in Θ and the thermal softening effect tends to compensate the strain and strain rate hardening effects. In the next phase of the evolution, Θ increases very slowly and the thermal softening effect becomes gradually stronger than strain and strain rate hardening effects, and the shear stress decreases very slowly as shown. Further evolutions of the stress and velocity profiles indicate unstable development, i.e. the shear stress at $y = 0$ is decreasing rapidly and the two halves of the slab (corresponding to $H \geq y > 0$ and $-H \leq y < 0$) are shearing relative to each other increasingly like rigid bodies. The instability can be seen more clearly by observing the evolution of shear stress and plastic strain rate at $y = 0$. The latter varies gradually and unremarkably up to $t = 60\mu$s, and shortly after which time, suddenly and steeply, i.e. by about five orders of magnitude in less than 0.5μs. After reaching the peak value of 5.3145×10^5 at $t = 60.8385\mu$s, the plastic strain rate quickly drops to a value very close to zero (i.e. 674 compared with the peak value of 5.3145×10^5) before showing a very small and slow increase, followed quickly by another sharp rise to a second peak (14.865×10^5) nearly three times the first one. Although the stress decreases rapidly and the plastic strain rate increases even more rapidly, the evolution is smooth and therefore it is not possible to define the onset of instability uniquely. Here we define the onset of the strain localization instability as the point when the rate of change of stress with time continues to increase monotonically and rapidly. We detect this point by examining the ratio P defined as $P = \frac{ds}{dt}|_{t_{n+1}} / \frac{ds}{dt}|_{t_n}$, for several time levels n. The instability is thus found to occur at $t = 60.407\mu$s. The interaction between the strain hardening and thermal softening effects, coupled with thermal diffusion and mechanical loading, gives rise to interesting mechanical response of the slab. The initially slow thermal diffusion, relative to the rate of mechanical loading, allows the thermal imperfection to cause local heating, which in turn causes thermal softening in a narrow band. As the thermal softening effect

grows stronger than the strain and strain rate hardening effects, the plastic strain rate increases sharply and the shear stress drops suddenly at the band centre. Thermal diffusion also becomes more extensive and the extent of the softened material propagates outwards. Continued shearing of the slab after the onset of strain localization exhibits more interesting interaction between thermal softening and strain and strain rate hardening effects, giving rise to apparent elastic unloading in the neighbourhood of $y = 0$ while plastic deformation continues on either sides of the band centre. However, high rate of plastic deformation quickly resumes as shown by the same figures.

We use six discretisations ($\{N_i\}_{i=1}^{p=6} = \{61, 101, 141, 181, 221, 261\}$ uniformly spaced collocation points, i.e. spacing $h_i = 1/N_i$), to study the convergence of our method. Due to a lack of exact solution, an estimate of "error" is computed as follows. For each level of discretisation, the governing equations are integrated to a specified time instant just after the onset of localisation ($t = 60.507\mu$s) to obtain the spatial profile of the temperature at this time instant. Then the temperatures at $Q = 300$ points are computed by interpolation (i.e. by the close form RBFN just found) and the discrete relative L_2 error is computed as $N_e = \sqrt{\sum_{j=1}^{Q}(\Theta_j^i - \Theta_j^p)^2}/\sqrt{\sum_{j=1}^{Q}(\Theta_j^p)^2}, \quad i = 1, 2, \ldots, p-1$, where $p = 6$. The result shows that the "error" is proportional to $O(h^{2.48})$. If we set the error at 10^{-2}, we would need 143 collocation points to discretise the domain. In comparison, Batra and Zhang [6] used 442 nodes in their investigation by the FE and MSPH methods.

Conclusion

The present meshless IRBFN method is an effective and efficient numerical method for the analysis of the strain localization in an elasto-thermo-visco-plastic slab under simple shearing. With a new coordinate mapping, the method only needs a relatively small number of computational degrees of freedom, distributed uniformly in the computational domain, to achieve a very high resolution of the spatial structure of the resultant localised shear band, which is caused by the combined effects of strain and strain rate hardening, thermal softening, and some thermal imperfection in the initial conditions of the material. The present results are compared favourably with those of the Modified Smooth Particle Hyrodynamics method [6]. The application of the present method to two- and three-dimensional strain localisation problems will be carried out in our future work.

Acknowledgement

The support for this work by the Australian Research Council is gratefully acknowledged.

References

[1] J. W. Walter Jr. Numerical experiments on adiabatic shear band formation in one dimension. *International Journal of Plasticity*, 8:657–693, 1992.

[2] A. Bayliss, T. Belytschko, M. Kulkarni, and D. A. Lott-Crumpler. On the dynamics and the role of imperfections for localization in thermo-viscoplastic materials. *Modelling and Simulation in Materials Science and Engineering*, 2:941–964, 1994.

[3] T. W. Wright and J. W. Walter. On stress collapse in adiabatic shear bands. *Journal of Mechanics and Physics of Solids*, 35:701–720, 1987.

[4] R. C. Batra and C. H. Kim. Effect of thermal conductivity on the initiation, growth and bandwidth of adiabatic shear bands. *International Journal of Engineering Science*, 29:949–960, 1991.

[5] Shaofan Li and Wing Cam Liu. Numerical simulation of strain localization in inelastic solids using mesh-free method. *International Journal for Numerical Methods in Engineering*, 48:1285–1309, 2000.

[6] R. C. Batra and G. M. Zhang. Analysis of adiabatic shear bands in elasto-thermo-viscoplastic materials by modified smooth-particle hydrodynamics (sph) method. *Journal of Computational Physics*, 201:172–190, 2004.

[7] E. J. Kansa. Multiquadrics – a scattered data approximation scheme with applications to computational fluid dynamics – ii. solutions to parabolic, hyperbolic and elliptic partial differential equations. *Computers & Mathematics with Applications*, 19:147–161, 1990.

[8] W. R. Madych and S. A. Nelson. Multivariate interpolation and conditionally positive definite functions, ii. *Mathematics of Computation*, 54:211–230, 1990.

[9] N. Mai-Duy and T. Tran-Cong. Numerical solution of differential equations using multiquadric radial basic function networks. *Neural Networks*, 14:185–199, 2001.

[10] N. Mai-Duy and T. Tran-Cong. An efficient indirect rbfn-based method for numerical solution of pdes. *Numerical Methods for Partial Differetial Equations*, 21:770–790, 2005.

[11] E. J. Kansa, H. Power, G. E. Fasshauer, and L. Ling. A volumetric integral radial basis function method for time-dependent partial differential equations: I formulation. *Engineering Analysis with Boundary Elements*, 28:1191–1206, 2004.

[12] Leevan Ling and Manfred R. Trummer. Multiquadratic collocation method with integral formulation for boundary layer problems. *Computers & Mathematics with Applications*, 48:927–941, 2004.

[13] N. Mai-Duy and T. Tran-Cong. Solving biharmonic problems with scattered-point discretization using indirect radial-basis-function networks. *Engineering Analysis with Boundary Elements*, 30:77–87, 2006.

[14] N. Mai-Duy. Solving high order ordinary differential equations with radial basis function networks. *International Journal for Numerical Methods in Engineering*, 62:824–852, 2005.

[15] N. Mai-Duy and R. I. Tanner. Solving high order partial differential equations with indirect radial basis function networks. *International Journal for Numerical Methods in Engineering*, 63:1636–1654, 2005.

[16] N. Mai-Duy and T. Tran-Cong. Approximation of function and its derivatives using radial basis function networks. *Applied Mathematical Modeling*, 27:197–220, 2003.

[17] E. Hairer and G. Wanner. *Solving Ordinary Differential Equations II. Stiff and Differential-Algebraic Problems*. Springer-Verlag, 1996.

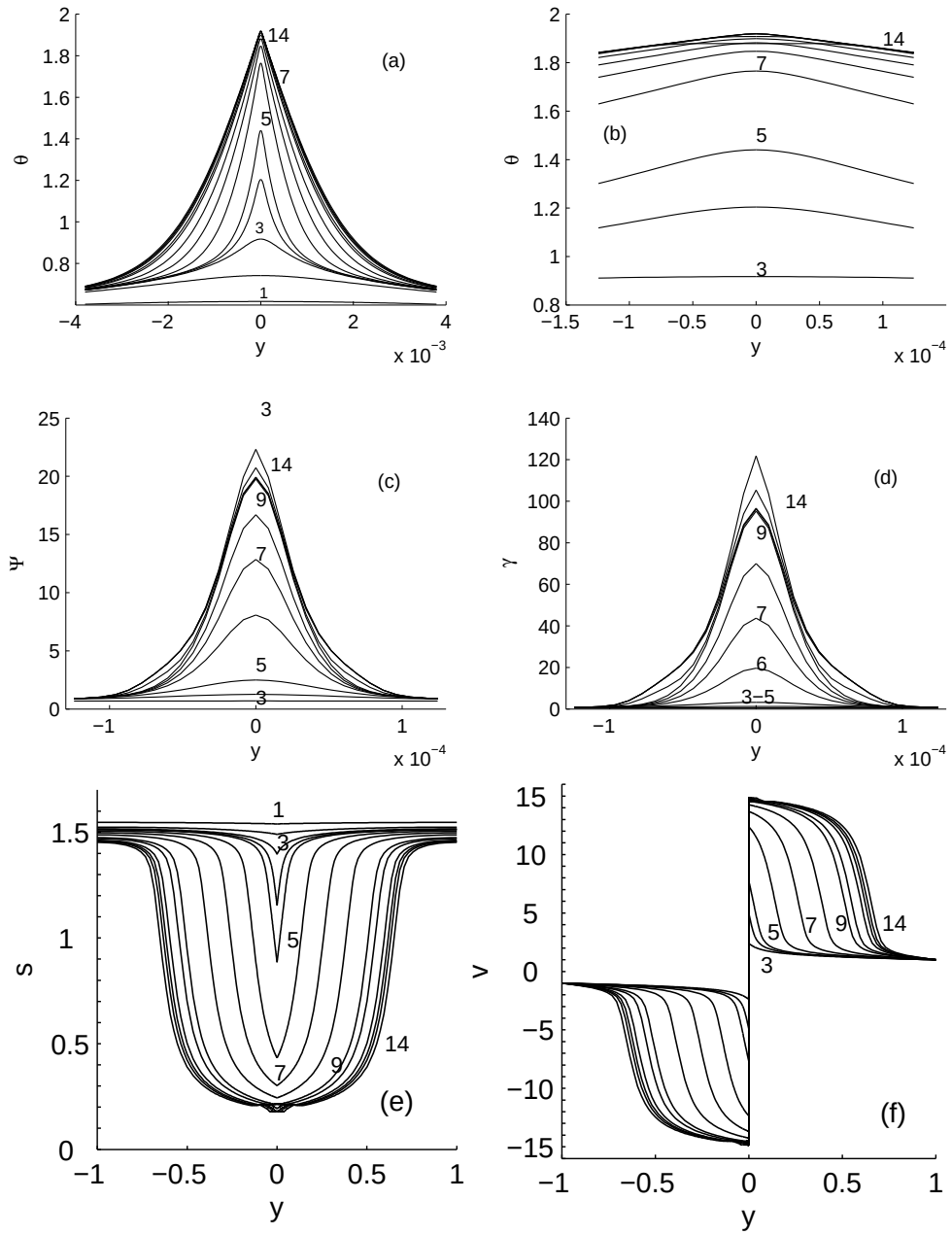

Figure 2: The curve labels indicate time levels (μs): 1(59.489); 2(60.257); 3(60.433); 4(60.477); 5(60.507); 6(60.602); 7(60.702); 8(60.804); 9(60.903); 10(60.934); 11(60.975); 12(60.992); 13(61.003); 14(61.019). Evolution of (a) temperature, (c) Ψ, (d) plastic train, (e) stress, and (f) temperature. (b) The temperature solution is highly consistent with the boundary conditions at $y = 0$.